An open-source numerical laboratory to assess the poromechanical behavior of fractured rocks

Ana Carolina Loyola, Manoel Porfírio Cordão Neto, Jean-Michel Pereira

Computers and Geotechnics 168 (2024) 106127

Contents lists available at ScienceDirect

Computers and Geotechnics

journal homepage: www.elsevier.com/locate/compgeo

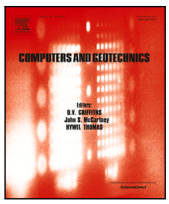

Research paper

An open-source numerical laboratory to assess the poromechanical behavior of fractured rocks

Ana Carolina Loyola [a,*], Manoel Porfírio Cordão Neto [b], Jean-Michel Pereira [a]

[a] Navier, Ecole des Ponts, Univ Gustave Eiffel, CNRS, Marne-la-Vallée, France
[b] Departamento de Engenharia Civil e Ambiental, Faculdade de Tecnologia, Universidade de Brasília, Brasília, Brazil

ARTICLE INFO

Keywords:
Open-source code
Finite volume method
Upscaling
Fractured media
Interface elements
Poromechanics
Elastoplasticity

ABSTRACT

The impact of fractures on the behavior of rock masses is frequently assessed with numerical methods for hydromechanical modeling and upscaling. Given the popularity of these methods, they can benefit from an open-source environment for their development. This paper introduces DuMu^x FracLab, a new module of the open-source software DuMu^x that extends the original code, already robust for solving flow and transport in porous media, to support poromechanical analyses in elastoplastic fractured media using the Box method with zero-thickness interface elements for discretization of the porous fractured domain. Novel features include the solution of elastoplastic problems with the Box method and functions that facilitate homogenization and the upscaling of properties with different boundary conditions. Notably, the imposition of periodic boundary conditions is made using a recent methodology based on the mortar method that we adapted for triple-node interfaces. We present the mathematical formulation, the design and main features behind DuMu^x FracLab as well as validation tests. Finally, two numerical examples demonstrate possible applications. The first one deals with the upscaling of stochastic fractured media and the second one reproduces the permeability history of a fractured chalk sample submitted to depletion and extension.

1. Introduction

Fractures can have a significant impact on the behavior of rock masses by serving as preferential paths or barriers for fluid flow, acting as planes of weakness and affecting compressibility, for example. The strongly coupled and non-linear hydromechanical behavior of fractures has been verified in pioneering experimental works (e.g., Barton et al., 1985) and is of important consideration to activities such as oil and gas extraction, geothermal energy exploitation, nuclear waste disposal, among others (Rutqvist and Stephansson, 2003).

The assessment of the poromechanical behavior of fractured rock masses heavily relies on numerical modeling, which has been applied to coupled hydromechanical problems such as fault reactivation (e.g, Rutqvist et al., 2013), hydraulic fracturing (Chen et al., 2022), and fluid production in fractured reservoirs (e.g., Tao et al., 2011; Gan and Elsworth, 2016). Apart from these large-scale problems, numerical modeling of fractured media is also used to evaluate the behavior of fractured samples. Frequently, these simulations aim to extrapolate information to large-scale problems, in which considering the impact of small-scale fractures is crucial but the computational cost of explicitly representing all of them is prohibitive. Techniques such as numerical homogenization (e.g., Massart and Selvadurai, 2012; Khoei et al., 2023) and numerical upscaling (e.g., Pouya and Ghoreychi, 2001; Pouya and Fouché, 2009; Castro et al., 2023) can be employed for this purpose.

Numerical upscaling, specifically, is widely used in various types of heterogeneous media. Although the term upscaling may refer to different techniques for transferring information between scales, we use it here as a synonym of computing equivalent constitutive properties by submitting a sample with a given microstructure to a set of constraints that can be either Dirichlet, Neumann or periodic boundary conditions. It is well-established that the choice of boundary conditions influences the upscaled properties' values, with Dirichlet and Neumann conditions providing upper and lower limits, respectively (Chalon et al., 2004; Pouya and Fouché, 2009) while periodic conditions return intermediary values. In numerical homogenization studies, periodic boundary conditions are often preferred due to their reported requirement of smaller sample sizes to converge to the final constitutive properties values (Terada et al., 2000; Miehe, 2003). However, imposing such boundary conditions on non-symmetrical domains is not straightforward and has been the focus of various works that developed new methods for this purpose (e.g., Larsson et al., 2011; Nguyen et al., 2012; Reis and Andrade Pires, 2014).

* Corresponding author.
E-mail address: analoyolacr@gmail.com (A.C. Loyola).

https://doi.org/10.1016/j.compgeo.2024.106127
Received 2 October 2023; Received in revised form 5 January 2024; Accepted 25 January 2024
Available online 2 February 2024

In summary, the numerical modeling of fractured media hinges on key factors such as the constitutive laws for fractures, hydromechanical coupling, and scale-transfer issues. Addressing these aspects requires the implementation of experimentally verified constitutive laws and on the use of thoroughly validated computational tools. On this last matter, there is a variety of softwares applicable to fractured media studies, including commercial ones like Abaqus (e.g JianPing et al., 2015) and UDEC (e.g Esmaieli et al., 2010), and open-source codes, with notable examples being OpenGeoSys (Bilke et al., 2022) and DuMu^x (Koch et al., 2020).

Open-source codes have significant potential for fast development due to the collaborative work fostered by the principles of free and open-source software. DuMu^x, in particular, is a C++ code well-equipped to solve multi-compositional, multi-phase and multi-physics flow and transport in porous media with different finite-volume discretization schemes. The computation of flow in fractured media is supported in its module for multi-domains, where fractures are represented as interface elements, and has been verified in benchmark studies (Flemisch et al., 2018; Berre et al., 2021).

However, DuMu^x has certain limitations when applied for mechanical problems. The geomechanics module, for instance, supports only linear elasticity and does not function with interface elements. Although there is an external module dedicated to deformable elastic fractured media (Gläser, 2020), its approach, centered on contact problems, overlooks crucial aspects of fracture mechanics, such as fracture stiffness and its non-linear character (Goodman et al., 1968; Bandis, 1980).

In this work, we introduce a new DuMu^x module called DuMu^x FracLab https://gitlab.com/navier-fraclab/dumux-fraclab, which significantly extends the original code by making it capable of solving history-dependent poromechanical problems on elastoplastic fractured media using the Box method with interface elements. Proposed by Helmig (1997), the Box method combines the mesh flexibility given by the shape functions of the Finite Element Method (FEM) with the local fluid mass conservation assured by Finite Volume Methods (FVM). Thus, it is efficient for solving flow and transport problems in complex geometries. In DuMu^x FracLab, the Box method is employed for the first time in elastoplastic analyses with the Mohr–Coulomb criterion, other plastic models being easily implementable.

DuMu^x FracLab is also conceived to facilitate the upscaling and homogenization of fractured media. It contains methods for computing volume averages and upscaled constitutive tensor with different boundary conditions, including the mortar periodic boundary conditions proposed by Reis and Andrade Pires (2014) for general meshes, which we adapted in this work to meshes that contain triple-nodded interface elements. Also, the computation of the volume averages employs the formulation by Pouya and Fouché (2009), who corrected previous errors in the classical formulation by Long et al. (1982) to compute the homogenized fluid velocity. This is a combination of methods that makes DuMu^x FracLab current and unique in handling the upscaling of fractured porous media.

Considering its functionalities, DuMu^x FracLab is useful for the broad community that is interested in numerical uspscaling or in coupled poromechanical models for fractured media. Also, it provides an open-source environment for the development and adaptation of problems that use interface elements for the discretization of fractures, whose current popularity is greatly due to new formulations (Segura and Carol, 2008b; Pouya, 2015; Cerfontaine et al., 2015; Martínez et al., 2022; Cui et al., 2019; Liaudat et al., 2023) that made the original interface by Goodman et al. (1968) applicable to a variety of coupled problems.

The following sections present the theoretical basis, the code structure, and applications of DuMu^x FracLab. Section 2 introduces the formulation of the poromechanical problem, the implemented constitutive laws, and the methods employed for discretization, homogenization, and the imposition of periodic boundary conditions on general meshes with interface elements. Section 3 presents the framework of a DuMu^x problem, the main extensions added in DuMu^x FracLab, and its design principles. Section 4 presents the validation tests made for the new implementations, and Section 5 presents two numerical examples. The first example demonstrates the potential use of DuMu^x FracLab to study the size effects and the influence of the chosen boundary conditions on the upscaled constitutive tensors of stochastic fractured media. The second example demonstrates how DuMu^x FracLab can be used to assess permeability changes due to fracture deformation by reproducing the laboratory experiments by Teufel et al. (1993) on a fractured chalk sample. Finally, Section 6 presents concluding remarks and discusses current limitations and perspectives.

2. Mathematical description and methods

We consider the problem of one-phase fluid flow coupled with mechanics in a fractured porous domain $\Omega = \Omega_m \cup \Omega_f$, where $\Omega_m \in \mathbb{R}^d$ is the porous matrix domain, d is the problem's spatial dimension and $\Omega_f \in \mathbb{R}^{d-1}$ is the lower-dimensional fracture domain, formed by a set of fracture surfaces Γ_j with sides $\Gamma_j^+ \in \Omega_f^+$ and $\Gamma_j^- \in \Omega_f^-$. In this scenario, the formulation of the hydromechanical boundary value problem (BVP), assuming small deformations, comprises the following equations for linear momentum balance and for the mass conservation of fluid in the porous matrix and in the fractures:

$$\sigma'_{ij,j} - bp_{,i} + b_i = 0 \text{ in } \Omega_m \tag{1}$$

$$\frac{1}{M}\dot{p} + b\dot{\varepsilon}_v + v_{i,i} + q = 0 \text{ in } \Omega_m \tag{2}$$

$$\frac{w}{M^f}\dot{p}^f + b^f\dot{w} + v_{i,i}w - q^{t+} - q^{t-} = 0 \text{ in } \Omega_f \tag{3}$$

On the internal boundaries of Ω_m that coincide with fractures, (1) is subjected to:

$$R_{ij}(t'_j - b^f p^f m_j) \text{ on } \Omega_m \cap \Omega_f \tag{4}$$

and, considering the domains $\Omega_f^+ \ni \Gamma_j^+$ and $\Omega_f^- \ni \Gamma_j^-$, with $\Omega_f = \Omega_f^+ \cup \Omega_f^-$, Eq. (2) is subjected to:

$$\begin{aligned} &q^{t+} \text{ on } \Omega_m \cap \Omega_f^+ \\ &q^{t-} \text{ on } \Omega_m \cap \Omega_f^- \end{aligned} \tag{5}$$

Here, $\boldsymbol{\sigma}'$ is the effective stress tensor in the porous matrix and $\boldsymbol{t}'$ is the effective stress vector in the fractures planes. The components of vector $\boldsymbol{t}'$ are written according to the local coordinate system ($\boldsymbol{n}\ \boldsymbol{t_1}\ \boldsymbol{t_2}$) defined by the fracture surface (Fig. 1), its first element being the normal stress σ_n so that $\boldsymbol{m} = \{1\ 0\ 0\}^T$. The rotation matrix $\boldsymbol{R}$ transforms the fracture's local coordinate system to the problem's global coordinate system, and is implemented according to the formulation by Cerfontaine et al. (2015). Also, $\mathbf{v}$ is the fluid's velocity vector, p is the fluid pressure, b and M are the Biot coefficient and Biot modulus, respectively. When these variables appear with the superscript f, they refer to the fracture domain. Moreover, ε_v is the porous matrix volumetric strain, w is effective fracture aperture, q is an external flux source and q^{t+} and q^{t-} are the exchange fluxes between the matrix and the fracture, computed at sides Γ_j^+ and Γ_j^- of the fracture surface as:

$$\begin{aligned} q^{t+} &= K_t(p^f - p^+) \\ q^{t-} &= K_t(p^f - p^-) \end{aligned} \tag{6}$$

where K_t is the fracture's transversal conductivity, and p^+ and p^- are the porous matrix fluid pressures on $\Omega_m \cap \Omega_f^+$ and $\Omega_m \cap \Omega_f^-$, respectively.

2.1. Constitutive laws

We present hereinafter the main constitutive laws available in DuMu^x and implemented in DuMu^x FracLab for the modeling of poromechanical problems.

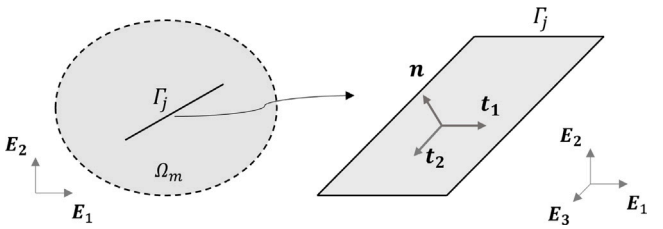

Fig. 1. Local coordinate system ($\boldsymbol{n}$ $\boldsymbol{t}_1$ $\boldsymbol{t}_2$) of a fracture Γ_j inside a domain Ω_m defined with a global coordinate system ($\boldsymbol{E}_1$ $\boldsymbol{E}_2$ $\boldsymbol{E}_3$).

The default constitutive law for fluid flow in porous media is Darcy's law:

$$v_i = \frac{k}{\mu}(p_{,i} - \rho g_i) \tag{7}$$

where k is the medium's intrinsic permeability, μ and ρ are the viscosity and density of the fluid, respectively and $\boldsymbol{g}$ is the gravity vector.

When in the elastic regime, the effective stresses in the porous matrix are a function of the matrix deformation tensor ε_{ij}:

$$\sigma'_{ij} = \lambda\delta_{ij}\varepsilon_{ij} + 2G\varepsilon_{ij} \tag{8}$$

where λ is Lamé's first parameter and G is the elastic shear modulus. At the fractures, the effective stress vector $\boldsymbol{t}'$ is defined as a function of the displacement jumps $[[\boldsymbol{u}]]$ across their plane as:

$$\boldsymbol{t}'^T = \{\sigma'_n \ \sigma_{t1} \ \sigma_{t2}\} = \boldsymbol{C}_f[[\boldsymbol{u}]] = \begin{bmatrix} K_n & K_{nt} & K_{nt} \\ K_{nt} & K_{t1} & 0 \\ K_{nt} & 0 & K_{t2} \end{bmatrix} \begin{Bmatrix} [[u_n]] \\ [[u_{t1}]] \\ [[u_{t2}]] \end{Bmatrix} \tag{9}$$

where $\boldsymbol{C}_f$ is the fracture stiffness matrix, formed by the fracture's normal stiffness K_n, the elastic dilatant stiffness K_{nt} and the tangential stiffnesses K_{t1} and K_{t2}. These fracture stiffnesses and the elastic moduli of the porous matrix can be state-dependent. In the case of the fractures, their normal stiffness is acknowledged to be highly dependent on their current state and is well-represented by non-linear functions such as the classical Barton-Bandis law (Bandis, 1980; Barton et al., 1985), by which the normal stiffness of a closing fracture is a function of its aperture.

If the material is elastoplastic, the yield surface provides a border for the stresses estimated in (8) and (9). In DuMu^x FracLab, the Mohr–Coulomb criterion is available for both the porous matrix and the fractures. For the porous matrix, we use the formulation by Nayak and Zienkiewicz (1972) written in terms of stress invariants:

$$p' \sin(\phi) + \sqrt{J_2}\left(\cos(\theta) - \frac{1}{\sqrt{(3)}}\sin(\theta)\sin(\phi)\right) - c\cos(\phi) = 0 \tag{10}$$

where c and ϕ are the porous matrix cohesion and friction angle, respectively. The invariant p' of the effective stress tensor σ'_{ij} is:

$$p' = \frac{1}{3}\sigma'_{ii} \tag{11}$$

and the Lode angle θ is defined by

$$-30° \le \theta = \frac{1}{3}\arcsin\left(\frac{-3\sqrt{3}\ J_3}{2J_2^{3/2}}\right) \le 30° \tag{12}$$

where J_2 and J_3 are invariants of the deviatoric stress tensor s_{ij}:

$$s_{ij} = \sigma_{ij} - \frac{\sigma_{kk}}{3}\delta_{ij} \tag{13}$$

$$J_2 = \frac{1}{2}s_{ij}s_{ij} \tag{14}$$

$$J_3 = \det(\boldsymbol{s}) \tag{15}$$

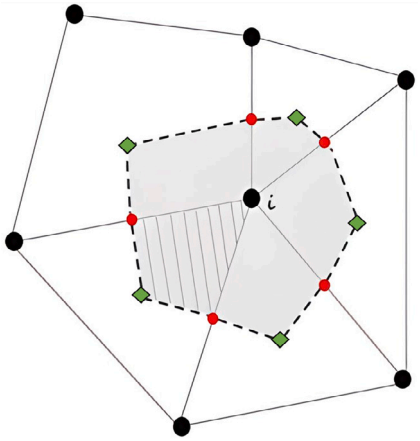

Fig. 2. The box discretization method: definition of a control volume of a node i of a primary finite element mesh. The hatched area represents a sub-control volume and the dashed lines are faces. The faces connect the centroid of the element edges (red circles) and of the sub-control volumes (green diamonds).

At the fracture planes, the Mohr–Coulomb criterion reads:

$$|\tau| - \sigma'_n \tan(\phi_f) - c_f = 0 \tag{16}$$

where ϕ_f and c_f are the fracture's friction angle and cohesion, respectively and the shear stress $\tau = \sqrt{\sigma_{t1}^2 + \sigma_{t2}^2}$.

DuMu^x FracLab implements a non-associative strain-hardening Mohr–Coulomb, in which cohesion, friction angle and dilation angle can be a function of a user-specified hardening variable.

2.2. Discretization

The discretization of both the mechanical and the flow problems is made with the Box method Helmig (1997), which consists of building control volumes around the nodes of a primary finite element mesh (Fig. 2). Stresses and fluxes are computed at the edges of the control volumes, called faces. The storage term is computed at the centroids of the sub-control volumes.

For the discretization of the fractures, we use the triple-nodded lower-dimension interface elements illustrated in Fig. 3. Note that the middle lower dimension element is only used by the flow problem to compute the fluid pressure in the fracture, while the edge nodes are used to compute pressures and displacements in the porous matrix. For the flow problem, the edge nodes are coupled to the middle ones by the exchange flux in (6).

2.3. Fixed-stress split

DuMu^x FracLab handles the hydromechanical coupling of the problem described in (1)–(3) with a sequential coupling scheme called the fixed-stress split. The use of a sequential coupling scheme allowed us to better respect the modularity of the original code and is more convenient for the future implementation of new solution methods specific to one of the coupled models. The comparative study by Kim et al. (2011) showed that the fixed-stress split is an interesting alternative to full-coupling since it offers unconditional stability, faster convergence, and more accurate results than other sequential coupling schemes.

In the fixed-stress split, the flow and mechanical problems are solved sequentially, in this order, until a criterion of convergence ε_{tol} is reached. During the resolution of the flow equation at a given iteration k of a time step t, the displacements and the strains are not known because the mechanical equation has not yet been solved. As a solution,

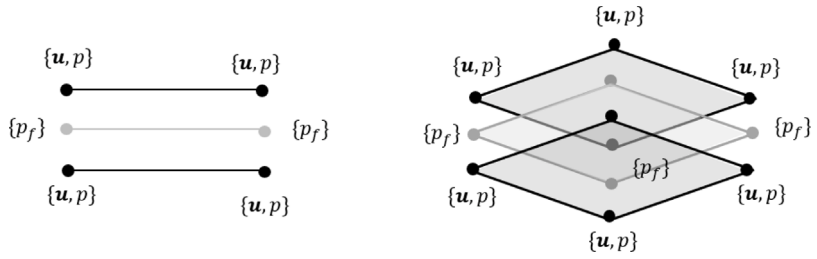

Fig. 3. Example of triple-nodded interface elements for 2D (left) and 3D (right) hydromechanical problems. The fracture pressure p_f is evaluated at the middle nodes and the fluid pressure p and displacements $\boldsymbol{u}$ in the porous matrix are evaluated at the edge nodes.

the volume strain and aperture variations are replaced by the following estimators:

$$d\hat{\varepsilon}_v^k = d\varepsilon_v^{k-1} + \frac{b^2}{K_{dr}}(p^{k,t} - p^{k-1,t}) \tag{17}$$

$$d\hat{w}^k = dw_v^{k-1} + \frac{b_f^2}{K_f}(p_f^{k,t} - p_f^{k-1,t}) \tag{18}$$

where K_{dr} and K_f are the bulk modulus of the porous matrix and the fracture. Selecting the adequate value for these moduli is highly important for convergence and a proper estimation depends on the dimensions of the problem and on the elastic or elastoplastic parameters. We adopt for K_{dr} the values suggested by Castelletto et al. (2015) and Kim et al. (2011) for elastic and elastoplastic 2D and 3D problems to obtain optimal convergence. For the fractures, K_f is equal to their normal stiffness.

We present below the essential steps of the algorithm for a time step t and iteration k:

1. Solve the flow Eqs. (2) and (3) using the estimators (17) and (18).
2. With the updated fluid pressure values, solve the mechanical equilibrium Eq. (1) and compute the actual values of $d\varepsilon_v^k$ and dw^k:

$$d\varepsilon_v^k = u_{i,i} \tag{19}$$

$$dw^k = [[u_n]] \tag{20}$$

   where u_i denotes the computed displacement increment vectors and $[[u_n]]$ denotes the normal displacement jump across the fractures planes.
3. Proceed to the next time step if:

$$\frac{\|\boldsymbol{p}^{k,t} - \boldsymbol{p}^{k-1,t}\|}{\|\boldsymbol{p}^{k,t}\|} \leq \varepsilon_{tol}$$
$$\frac{\|\boldsymbol{u}^{k,t} - \boldsymbol{u}^{k-1,t}\|}{\|\boldsymbol{u}^{k,t}\|} \leq \varepsilon_{tol} \tag{21}$$

   Otherwise, begin a new iteration.

2.4. Numerical upscaling

The upscaled mechanical constitutive tensor $\boldsymbol{C}$ and permeability tensor $\boldsymbol{K}$ of a heterogeneous domain can be obtained by solving linearly independent systems of the type:

$$\langle \sigma'_{ij} \rangle = C_{ijkl}\langle \varepsilon_{kl} \rangle = \frac{1}{2}C_{ijkl}(\langle u_{k,l} \rangle + \langle u_{l,k} \rangle) \tag{22}$$

$$\langle v_i \rangle = K_{ij} : \langle p_{,j} \rangle \tag{23}$$

where $\langle \cdot \rangle = \frac{1}{V}\int_V \cdot dV$ and V is the volume of the domain. Using the divergence theorem, the volume integrals of displacement and pressure gradients can be converted to surface integrals as :

$$\int_V a_{,i} dV = \int_{\partial V} a n_i \, d\partial V \tag{24}$$

where the variable a is a general representation of either fluid pressure p or a directional component u_k of the displacement vector.

To compute the integral $\int_V v_i dV$ of the fluid velocity vector we use the following formulation by Pouya and Fouché (2009):

$$\int_V v_i dV = \int_{\partial V} (v_j n_j) x_i \, d\partial V + \sum_{k \in \partial\Omega_f} q^{(k)} x_i^{(k)} \tag{25}$$

where $\boldsymbol{x}$ is a position vector on ∂V, $\partial\Omega_f$ is the domain of fracture traces at the boundaries of V, i.e., the points (for 2D) or lines (for 3D) formed by the intersection of the fracture domain and the boundary ∂V; $q^{(k)}$ is the flow rate at trace k and $\boldsymbol{x}_i^{(k)}$ is the position vector of trace k.

Considering the classical Hill–Mandel principle for homogenization (Hill, 1972), in which body forces are neglected, this methodology can also be applied to compute $\int_V \sigma'_{ij} dV$ as:

$$\int_V \sigma'_{ij} dV = \int_{\partial V} (t_i n_i) x_j \, d\partial V + \int_V b p \delta_{ij} \, dV \tag{26}$$

where $\boldsymbol{t}$ is the vector of boundary tractions. Note that there are cases where it is important to consider inertia, body forces or dynamic effects when computing homogenized stresses. DuMu^x FracLab does not yet include this possibility, but the interested reader is referred to de Souza Neto et al. (2015) and Khoei and Hajiabadi (2018) for extended theories that consider these effects.

Numerical upscaling consists of imposing sets of linearly independent boundary conditions to solve several BVPs and compute the upscaled (apparent) constitutive tensors for a given microstructure. The boundary conditions types can be Neumann (stresses and fluxes), Dirichlet (displacement and pressures) or periodic.

The most common Neumann boundary conditions are the so-called constant traction and flux boundary conditions for mechanics and fluid flow, which set each component $\langle \sigma_{ij} \rangle$ and $\langle v_i \rangle$ to be non-zero at a time. And common Dirichlet boundary conditions are linear pressure and linear displacement boundary conditions, which set a configuration of the primary variables such that each gradient component $\langle p_{,i} \rangle$ and $\langle u_{i,j} \rangle$ is non-zero at a time.

Periodic conditions also impose pressure and displacement gradients, but this must be done respecting the constraint of periodicity for pressures and displacements:

$$p(\boldsymbol{x}^+) = p(\boldsymbol{x}^-) + \overline{p_{,i}}(x_i^+ - x_i^-) \tag{27}$$

$$u_i(\boldsymbol{x}^+) = u_i(\boldsymbol{x}^-) + \overline{u_{i,j}}(x_j^+ - x_j^-) \tag{28}$$

where $\boldsymbol{x}^+$ and $\boldsymbol{x}^-$ are coordinates of a pair of symmetric opposite boundary points (Fig. 4), $\overline{u_{i,j}}$ and $\overline{p_{,i}}$ are the imposed displacement and pressure gradients. Also, it is necessary to respect the constraint of anti-periodicity of flow rates Q and surface forces $\boldsymbol{T}$:

$$Q(\boldsymbol{x}^+) = -Q(\boldsymbol{x}^-) \tag{29}$$

$$\boldsymbol{T}(\boldsymbol{x}^+) = -\boldsymbol{T}(\boldsymbol{x}^-) \tag{30}$$

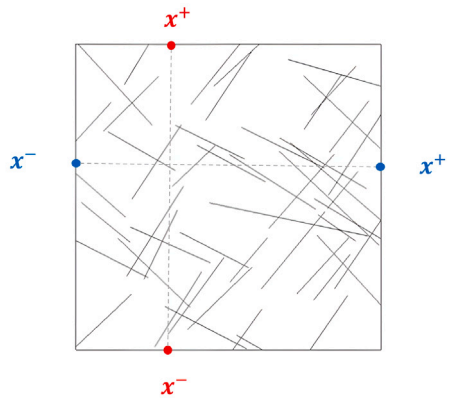

Fig. 4. Examples of pairs of opposite and symmetric boundary points in a two-dimensional domain. The conditions of periodicity and anti-periodicity are imposed on each of these pairs.

2.5. Mortar periodic boundary conditions

For the imposition of periodic boundary conditions on general 2D meshes with interface elements, DuMu^x FracLab uses and adapts the methodology proposed by Reis and Andrade Pires (2014). The essentials of this methodology will be presented below, with more information available in Reis and Andrade Pires (2014) and Rodrigues Lopes et al. (2021).

The boundaries of the domain are divided into a mortar (independent) and a non-mortar (dependent) side, which will be hereinafter indicated by the superscripts m and n, respectively. The main idea of the method is to enforce weakly the periodicity constraint (27)–(28) by solving:

$$\int_{\Gamma_i} (\pi_n(a^n) - \pi_m(a^m))\psi_n d\Gamma_i = \overline{a_{,j}}(x_j^n - x_i^m) \tag{31}$$

Here, a is a general denotation for a primary variable u_i or p, $\overline{a_{,j}}$ is its imposed gradient, and $\boldsymbol{x}$ is the position vector of a boundary point. The domain Γ_i is a "virtual integration line" built from the projection of the boundary nodes (Fig. 5). The functions π_m and π_n interpolate the variables at mortar and non-mortar nodes on $d\Gamma_i$ using the finite element shape functions. And the test functions ψ_n are the Lagrange multipliers proposed by Rodrigues Lopes et al. (2021).

The solution of (31) leads to a relationship of the following form:

$$a_i^n - A_{ij}a_j^m = \overline{a_{,k}}(x_k^n - x_k^m) \tag{32}$$

where $k = 1...2$, i and j are indexes of boundary nodes. Matrix $\boldsymbol{A}$ stores coefficients that determine the dependency of the non-mortar nodes on the mortar nodes that share common segments of the virtual integration line. A similar procedure to impose the anti-periodicity conditions (29) and (30) leads to:

$$f_j^n + A_{ij}^T f_j^m = 0 \tag{33}$$

where $\boldsymbol{f}$ denotes, generally, the vectors of forces and flow rates at the nodes and the superscript T denotes the transpose of a matrix.

Eqs. (32) and (33) introduce additional relationships that ensure the determinancy of the systems constituting the hydromechanical problem. Explicit enforcement of pressure and displacement boundary conditions is only required at one of the corners. Typically, in the mechanical problem, this corner is assigned zero displacements to prevent rigid body motion. In the flow problem, the corner can be constrained to a fluid pressure that appropriately represents the sample's state, if the problem is state-dependent.

This method can be readily applied to our mechanical problem with interface elements. In this case, the virtual line exhibits "discontinuities" that result in distinct dependency relationships for nodes along the same interface (Fig. 5). Consequently, there can be displacement discontinuities across interface boundary nodes, which removes the overstiffness associated with Dirichlet boundary conditions (Svenning et al., 2016). However, the flow problem requires additional constraints because it uses an additional domain of middle interface elements to compute fracture pressures (Fig. 3).

To address this, we propose an adaptation to enforce the periodicity conditions on this lower-dimensional domain. In this adaptation, the middle nodes at the boundaries become dependent on their correspondent nodes at the edges of the interface. If these middle nodes are located on the non-mortar side, they inherit the dependency of their coupled edge nodes, becoming indirectly dependent on the same mortar nodes.

Consider a fracture lower-dimensional domain Ω_f of boundary $\Gamma_f = \Gamma_f^m \cup \Gamma_f^n$. For a fracture node $i \in \Gamma_f$ that overlaps with a set of matrix nodes $C_m(i)$ located at the edges of the interface element, the periodicity condition becomes:

$$p_i^{\Gamma_f} - \alpha_{ij}p_j^m - \overline{p_{,k}}(x_k^{\Gamma_f} - x_k^m) = 0 \tag{34}$$

And the modified anti-periodicity constraint for the flow rate is:

$$q_j^m + A_{ij}^T q_j^n + \alpha_{ij}^T q_j^{\Gamma_f} = 0 \tag{35}$$

where

$$\alpha_{ij} = \begin{cases} \frac{1}{2}, & \text{if } i \in \Gamma_f^m \text{ and } j \in C_m(i) \\ \frac{1}{2}\sum_{j \in C_m(i)} \boldsymbol{A}_{jk}, & \text{if } i \in \Gamma_f^n \text{ and } j \in C_m(i) \\ 0, & \text{otherwise} \end{cases} \tag{36}$$

Note that (34)–(36) enforces the pressure at the middle node i to be equal to the average of the pressures of its correspondent edge nodes. Segura and Carol (2004) proposed the same enforcement to be able to capture pressure drops across the fracture without the need for triple-nodded interfaces. They demonstrated that this assumption holds well, except in cases where the fracture's permeability is significantly lower than that of the matrix. As we employ this assumption only at the boundaries, we anticipate that the impact of blocking fractures will still be captured within the domain's interior.

3. Code design

This section presents the general structure and the design principles of a DuMu^x simulation and describes the main extensions that form the new module DuMu^x FracLab.

3.1. Framework

The main components of a DuMu^x simulation can be identified in Fig. 6, which presents a general framework to build a new problem for flow in fractured media.

Tags are C++ structures used in DuMu^x to define several properties at compile time. To set the main properties of the new problem, the user must create a tag that inherits the properties of pre-existing DuMu^x tags (step 1). For example, a problem to solve fluid flow in fractured media can inherit from the tag *BoxFacetModel*, which sets a discretization with the Box method and triple-nodded interface elements, and from the tag *OneP*, which defines properties for one-phase flow problems.

The Problem and Spatial Parameters classes (steps 2 and 3) require the users to overload methods that define problem and material related features, such as initial and boundary conditions and constitutive properties, which can be space and solution-dependent. New classes can be used to define properties that do not have default types or redefine default types (step 4).

The Coupling Mapper class (step 7) is called and instantiated after building the finite-volume grid to create the triple-nodded interfaces and to map the matrix and fracture nodes that are coupled.

The Grid Variables classes are used to set, map and store the problem variables at the proper grid entities (nodes, sub-control volumes

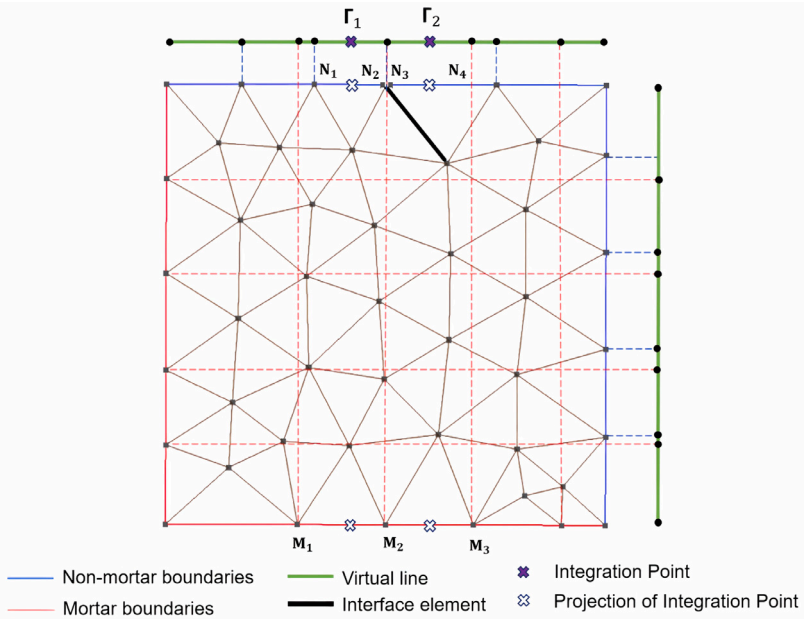

Fig. 5. Virtual integration lines built with the projection of the boundary nodes for the imposition of mortar periodic boundary conditions with the methodology proposed by Reis and Andrade Pires (2014). The periodicity constraints are integrated over these lines by mapping, with the finite element shape functions, their integration points on the mortar and non-mortar sides. In the figure, the non-mortar nodes N_2 and N_3 have equal coordinates because they belong to opposite sides of an interface elements. Despite of that, they have different dependencies because they create a discontinuity in the virtual integration line: while segment Γ_1 establishes a constraint relationship between nodes N1, N2, M1 and M2, the adjacent segment Γ_2 establishes a relationship between nodes N3, N4, M2 and M3.

1. Set problem tags
2. Set Spatial Parameters class
3. Set Problem class
4. Set Properties
5. Create primary mesh
6. Create Finite Volume mesh
7. Initialize Coupling Mapper
8. Initialize Grid Variables
9. Initialize Coupling Manager
10. Set Assembler and Solver classes
11. Assemble and solve system
12. Update Grid Variables
13. Write output

Fig. 6. Framework to define a problem of flow in fractured media in DuMu^x.

or faces). The grid variables should be initialized to set an initial state (step 8). Before solving the system, it is also necessary to set the Coupling Manager (step 9), which will handle the coupling of the fracture and the matrix domains by computing the exchange flux in (6).

The selected assembler (step 10) sets the residual vector and the tangent matrix with the perturbation method. To this end, it computes fluxes and forces at the grid entities using a tag-defined constitutive law, which is Darcy's law for problems derived from the tag *OneP* and Hooke's law for problems defined with the tags *Elastic* or *PoroElastic*. After solving the system (step 11), the grid variables are updated (step 12) to proceed to a new time step or to write the output in VTK format (step 13).

3.2. New implementations

DuMu^x FracLab is a new module that extends DuMu^x to handle the solution of hydromechanical problems on elastic and elastoplastic fractured media and facilitates the upscaling of hydromechanical properties. We present here the main new features that were implemented to achieve these objectives. Note that DuMu^x FracLab is composed of several more additions that can be consulted in the Doxygen documentation available in the Git repository.

The extensions in DuMu^x FracLab do not change the core framework in Fig. 6. Instead, they add new classes to be used in the steps of this framework. Most of these classes are already defined as default types in six new pre-defined tags: *Elastoplastic*, *Poroelastoplastic*, *InterfaceElastic*, *InterfacePoroelastic*, *InterfaceElastoplastic* and *InterfacePoroelastoplastic*, which are used for elastic and elastoplastic problems in media without or with interface elements.

In the assembly of the system (step 11) of mechanical problems, DuMu^x calls methods to compute stresses on all faces of each control volume. Previously, there were methods to compute stresses in bulk elements with Hooke's law (Eq. (8)) only. In DuMu^x FracLab there are new methods to compute stresses on faces that coincide with interfaces, using the elastic law in (9).

Also, there are new classes for stress computation in elastoplastic bulk elements and interfaces. They use an elastic law to compute the elastic trial, which by default is Hooke's law (8) for bulk elements and the law in (9) for interfaces. If this trial surpasses the yield surface, a user-defined class for the return algorithm is called to correct the stresses. In DuMu^x FracLab the only available plastic models are non-associated perfectly plastic and strain-hardening Mohr–Coulomb criteria, for which the two-vector return algorithm proposed by Crisfield (1987) is implemented.

When defining the properties of an elastoplastic problem, the user must define the new properties called *ReturnAlgorithm* and *InterfaceReturnAlgorithm*, if plastic interfaces exist. Thanks to this property, the classes for plastic correction are flexible to deal with any type of elastoplastic model without the need for internal changes.

To implement a new plastic model, it suffices to create two new classes: one for the constitutive law that defines yield, flow and hardening functions, and one for the return algorithm. Then, it would be necessary to define the return algorithm property as illustrated below.

```
template<class TypeTag>
struct ReturnAlgorithm<TypeTag,
    MyProblemTag>
{ using type = MyReturnClass;};

// if there are interfaces, also define
    return for them
template<class TypeTag>
struct InterfaceReturnAlgorithm<TypeTag,
    MyProblemTag>
{ using type = MyInterfaceReturnClass;};
```

Code Sample 1: Adding a new return algorithm property

DuMu^x FracLab also added to DuMu^x new Grid Variables classes that allow for the storage and update of stress and state-variables (steps 8 and 12), which was not possible before. Thanks to that, DuMu^x now supports an incremental formulation and can handle history-dependent mechanical problems.

Apart from the existing coupling manager (step 9) that couples the porous matrix to the fracture domain in flow problems, DuMu^x FracLab has three new types of coupling managers: (i) a coupling manager for mechanical problems in fracture media, which couples bulk elements that share an interface and compute their displacement jumps (ii) hydromechanical coupling managers that couple flow and mechanical problems with the fixed-stress split and (iii) coupling managers for the imposition of mortar periodic boundary conditions, which couple the mortar and non-mortar sides of the domain by building the mapping matrices ($\boldsymbol{A}$ and $\boldsymbol{\alpha}$ in (32) and (34)).

Finally, the new functionalities for homogenization and upscaling are introduced in a new sub-module called Homogenization, which contains classes that implement Eqs. (24)–(26) to compute the volume averaging of the gradients of primary variables, stresses and velocities. Also, there are new classes dedicated to the computation of the upscaled permeability and elastic compliance/stiffness tensors with Dirichlet, Neumann or mortar periodic (for 2D domains) boundary conditions. One needs to initialize these upscaling classes with the geometry of the domain to easily get upscaled properties using the following methods:

```
// get Upscaled properties. Boundary
    condition type is the argument
const auto perm = permUpscaling->
    getUpscaledPermeability("Dirichlet");
const auto comp = elasticUpscaling->
    getUpscaledComplianceTensor("Periodic")
    ;
```

Code Sample 2: A simple way of getting upscaled permeability and elastic tensors with a given type of boundary condition.

4. Validation tests

The new extensions in DuMu^x FracLab were validated by a series of numerical tests, which are all available in the Git repository. Five tests were conceived to validate the new implementations. They are:

- Test 1: Validates the implementation of the elastic laws for fractured media and of the homogenization functions.
- Test 2: Validates the implementation of the plastic correction and of the Mohr–Coulomb return algorithms for the porous matrix and the interfaces.
- Tests 3 and 4: Validate the implementation of the fixed-stress split for the porous matrix and the interfaces, respectively.
- Test 5: Verifies the implementation of the mortar periodic boundary conditions.

Table 1
Validation test 1: Elastic properties adopted for the porous matrix and for the fractures.

Matrix		Fracture		
E (MPa)	ν	K_n (MPa/m)	K_t (MPa/m)	K_{nt} (MPa/m)
50	0.25	50	10–50	0

4.1. Test 1: Upscaling of elastic properties of fractured media

To validate the implementation of elastic stress–strain laws for interfaces and of the homogenization methods, we computed the upscaled elastic properties of the idealized fractured domain described in Fig. 7, which contains persistent and regularly spaced sets of perpendicular fractures. Duncan and Goodman (1968) presented an analytical solution for the elastic compliance tensor of this fractured domain, and showed how the properties of different fracture orientations β can be obtained with tensor rotation.

In the numerical tests with DuMu^x FracLab, we upscaled the elastic compliance tensor with constant traction boundary conditions, which better represent the conditions of the analytical solution. We tested different values of β and of the fractures tangent stiffness K_t. Table 1 presents the adopted elastic properties for the porous matrix and the fractures.

Fig. 7 compares the analytical and numerical results. There is a good match between them, with a maximum observed error of 1.5%.

4.2. Test 2: Plastic correction and Mohr–Coulomb return

To validate the implementation of the return algorithm for the Mohr–Coulomb criterion, we performed numerical compression tests on 3D samples crossed by one fracture plane, such as the one illustrated in Fig. 8. Based on the Single Weakness Plane Theory (SWPT), Jaeger (1960) presented an analytical solution for the compression strength of this domain for different angles α between the fracture and the vertical direction. Both the fractures and the porous matrix follow a perfectly plastic Mohr–Coulomb criterion.

In the numerical model, an initial confinement stress is applied followed by displacement-controlled axial loading. The compression strength is considered to be the final homogenized axial stresses, which occurs when this value stabilizes. The criterion used for stabilization was a relative shift of less than 2% with respect to the initial axial stress variation that occurs in the elastic regime.

Fig. 8 exemplifies the geometry and the mesh for $\alpha = 55°$. We tested several values of α for a confinement stress σ_3 of 5 MPa and in uniaxial compression tests ($\sigma_3 = 0$). Table 2 presents the adopted strength parameters and Fig. 9 compares the compression strengths obtained with the analytical solution and with the model in DuMu^x FracLab. The numerical model could capture exactly the analytical strength for all tests cases. Note that depending on α and on the confinement stress, the compression strength can be dictated by the fracture or the rock matrix; thus, Test 2 validates the return algorithm for both the bulk and the interface elements.

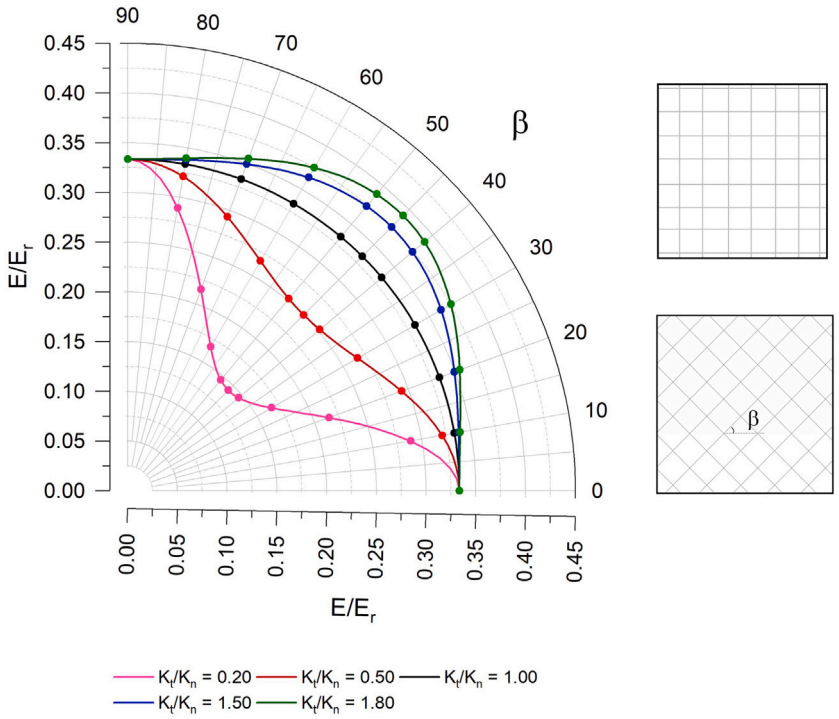

Fig. 7. Validation test 1: comparison between the analytical (lines) and numerical (dots) solutions of E/E_r, where E is the upscaled Young modulus of the fractured rock mass and E_r is the Young modulus of the intact rock.

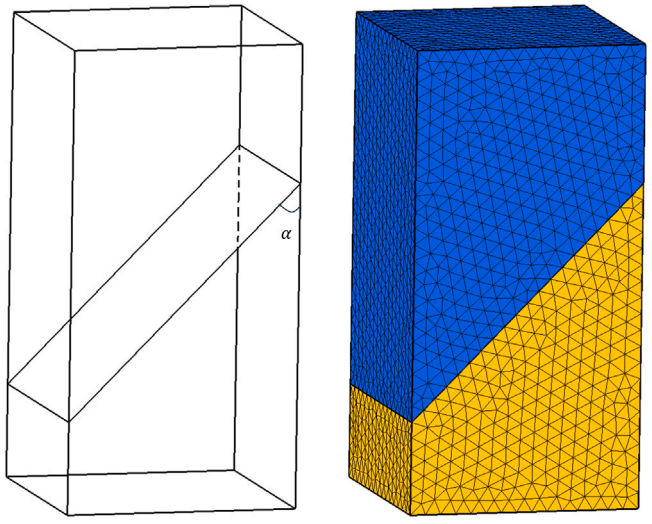

Fig. 8. Validation test 2: design of the sample crossed by one plane fracture of orientation α (left) and its mesh (right).

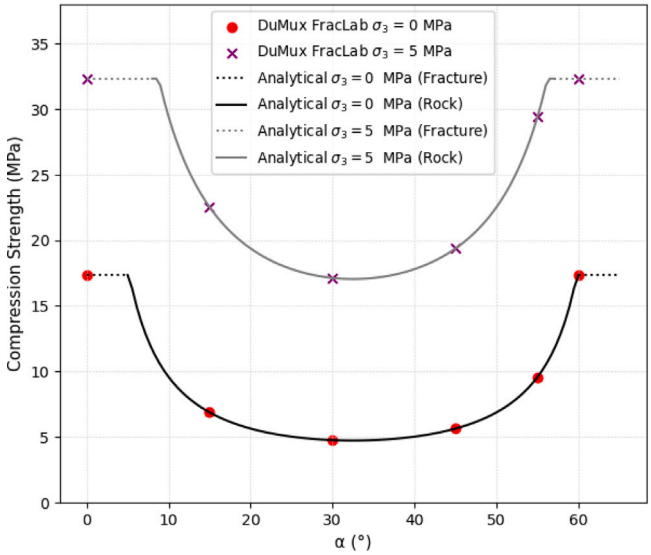

Fig. 9. Validation test 2: Comparison of the analytical and numerical compression strengths when applying a confinement stress σ_3 of zero (uniaxial compression test) and of 5 MPa. The plots for the analytical solution indicate whether failure occurs in the rock matrix or in the fracture.

Table 2
Validation test 2: Elastic and Mohr–Coulomb parameters adopted for the porous matrix and for the fractures.

Matrix				Fracture			
E (MPa)	ν	c (MPa)	ϕ (°)	K_n (MPa/m)	K_t (MPa/m)	c_f (MPa)	ϕ_f (°)
50	0.25	5	30	50	10	1.5	25

4.3. Tests 3 and 4: Hydromechanical coupling

The implementation of the fixed-stress split algorithm was validated for the bulk domain and the interfaces separately by reproducing Mandel's problem (Mandel, 1953) and the consolidation problem proposed by Segura and Carol (2008a). In both cases, we set the convergence criterion for the fixed-stress split (21) to $\varepsilon_{tol} = 0.001$.

Mandel's problem consists of a rectangular domain compressed both at the top and bottom boundaries by a load q, with drainage allowed to occur at the sides (Fig. 10). The initial pore pressure is $P_0 = -\frac{1}{3}q(1+\nu_u)$, where ν_u is the undrained Poisson's ratio. We adopt the same problem definitions used by Preisig and Prevost (2011): the domain is a 2m-side square, the load q is equal to 10 kPa and the material properties are those described in Table 3. Due to the symmetry of the problem, only a quarter of the domain needs to be simulated. The mesh has 400 linear squared elements and the total time of the simulation is 1 s, which is divided in 200 steps.

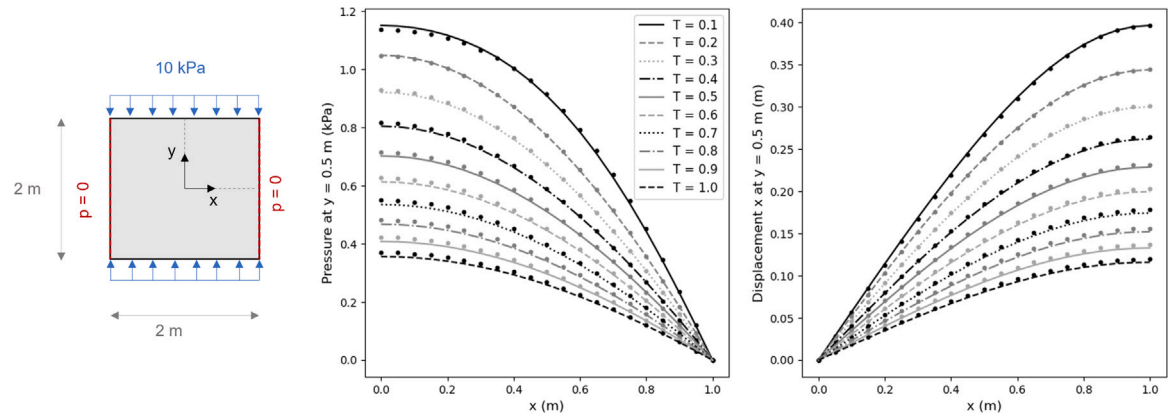

Fig. 10. Validation test 3 (Mandel's problem): On the left, the dimensions and boundary conditions of the problem. On the right, the comparison between the analytical (lines) and numerical (dots) solutions for pore pressures and displacements at different times T.

Table 3
Validation test 3 (Mandel's problem): Poroelastic parameters of the porous matrix.

E (kPa)	ν	ν_u	k_m (m/s)	b	M (kPa)
1.0	0.0	0.5	1.0	1.0	∞

Convergence was attained within two to three iterations per time step, resulting in a total of 439 iterations. Fig. 10 compares the analytical and numerical solutions for the distribution of the pressure and horizontal displacements along the line $y = 0.5$ m at different times. A maximum error of 3.9% was observed for these data.

Test 4 is the consolidation problem proposed by Segura and Carol (2008a) of a porous medium containing a permeable vertical fracture (Fig. 11). They used this test to verify their algorithm for sequential and full coupling one against the other. In this problem, the domain is initially at a constant pore pressure of 10 kPa because of a vertical loading of the same magnitude. Like in a classical Terzaghi consolidation problem, the top boundary is restrained to zero pressures, the bottom boundary to zero vertical displacements, and the lateral boundaries to zero horizontal displacements. The mesh contains 400 triangular bulk elements and 10 lower-dimensional linear elements to represent the fracture. A time step of 0.5 s was adopted. The parameters of the problem are described in Table 4.

Fig. 11 compares the pore pressure distribution for different times along the fracture obtained in DuMu^x FracLab and by Segura and Carol (2008a) using the two coupling approaches. Note that while we use triple-nodded interfaces, they employed two-nodded interfaces with the enforcement of the fractures pressure to be the average of the pressures at the matrix nodes. This latter assumption is supposed to work well for permeable fractures, as is the case here. Indeed, there is a good correspondence with the results obtained in DuMu^x FracLab. The effect of the fracture on the speed of consolidation can be verified by comparing this solution with the one for a classical Terzaghi's consolidation, which was also verified by Segura and Carol (2008a) and is available as an extra validation test in the DuMu^x FracLab repository.

4.4. Test 5: Mortar periodic boundary conditions

Periodic boundary conditions are expected to return the true effective properties of periodic domains with the homogenization of one unit cell only, while Dirichlet and Neumann boundary conditions require a number of unit cells to converge to the true effective properties.

Test 5 verifies if the adaptation made to the mortar periodic boundary conditions for triple-nodded elements returns the expected properties. For that, we upscaled the permeability tensor of the fractured periodic domain in Fig. 12, which is composed of a fractured unit cell that repeats itself. We tested domains that contain a grid of 1 x 1 cell to 40 x 40 cells using linear pressure, flux, and mortar periodic boundary conditions. The fracture intrinsic permeability is 3.5×10^{-10} m^2, while the matrix permeability is 1.0×10^{-15} m^2.

Table 4
Validation test 4: poroelastic parameters of the porous matrix and the fracture.

Matrix				
E (MPa)	ν	k_m (m/s)	b	M (MPa)
1.0	0.25	1.16×10^{-5}	1.0	∞
Fracture				
K_n (MPa/m)	w_0 (mm)	k_f (m/s)	b_f	M_f (MPa)
20.0	1.0	1.0	1.0	∞

Fig. 13 presents the upscaled components of the permeability tensors as a function of the number of cells. Indeed, the periodic boundary conditions require only one unit cell to yield the final properties. As also theoretically expected, linear pressure (Dirichlet) and flux (Neumann) boundary conditions provide upper and lower bounds for the upscaled properties, respectively.

Fig. 14 presents a comparison of the pore pressure fields of the unit cells submitted to a gradient in the x-direction using the three types of boundary conditions. In the periodic case, there is a zone of high-pressure gradient at the top right portion of the domain. It is due to the anti-periodicity constraint (29), which imposes the flux at the fracture node F1 to be equal to the flux at its opposite matrix node. Indeed, if this cell is repeated periodically, the tip of a permeable fracture is expected to have this effect, since it creates a zone of localized flow that rapidly drains the fluid pressure of the surrounding porous matrix. The other boundary conditions, however, cannot capture this interaction between adjacent fracture and matrix nodes with one unit cell only. They impose similar fluid pressures for the fracture nodes F1 and F2, which have different connectivities when considering the whole periodic structure.

5. Numerical examples

This section presents two examples of the type of study that can be conducted with DuMu^x FracLab, both being available in the Git repository. To highlight the functionalities added to facilitate homogenization, both examples focused on the assessment of the equivalent properties and of the hydromechanical behavior of fractured samples, but the code can be used to many other types of hydromechanical analyses of fractured media.

5.1. Example 1: Upscaling of stochastic fractured media

DuMu^x FracLab can be used to compare different upscaling boundary conditions and perform sample size studies to select the Representative Elementary Volume (REV).

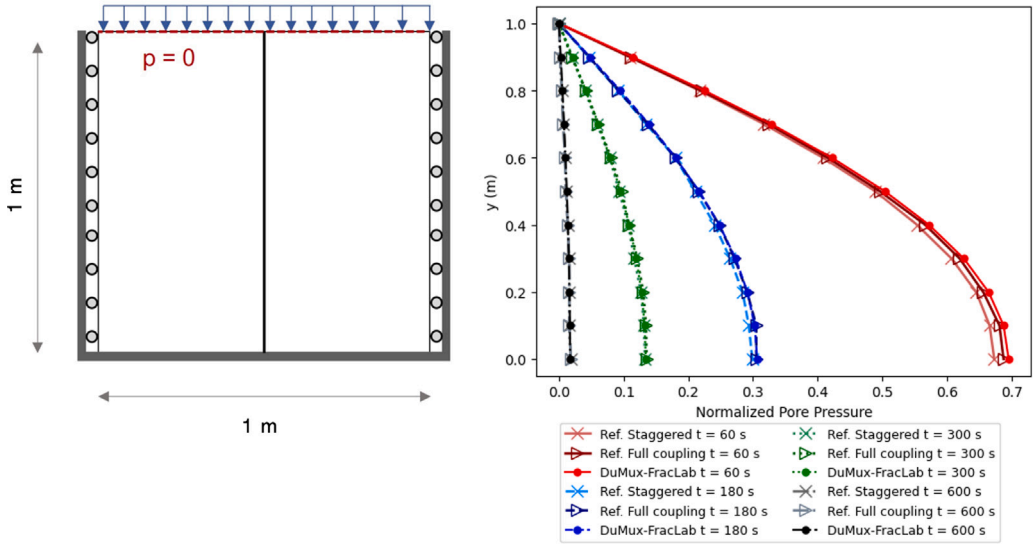

Fig. 11. Validation test 4: Consolidation problem conceived by Segura and Carol (2008a) on a squared domain containing a permeable vertical fracture (left) and comparison of their numerical results with a staggered and a fully coupled scheme with those obtained in DuMu^x FracLab with the fixed-stress split (right).

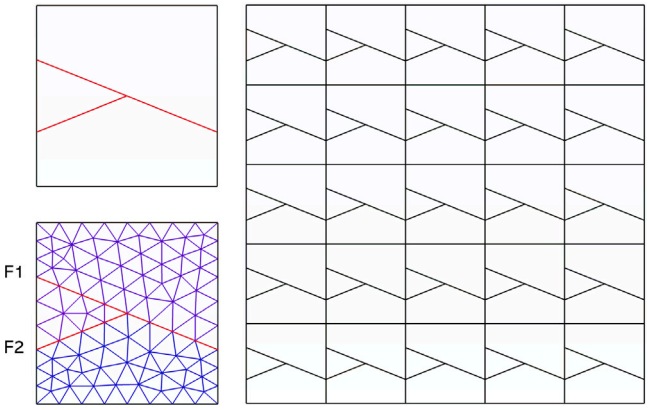

Fig. 12. Validation Test 5: On the left, the fractured unit cell that forms the periodic domain, and its adopted mesh. On the right, an example of a periodic domain formed by a grid containing 5 × 5 unit cells.

Table 5
Statistical parameters for Network 1, from Yang et al. (2014).

	Dip orientation			Length			Density
	Type	Mean(°)	Std. Dev.(°)	Type	Mean(m)	Std. Dev. (m)	(1/m^2)
Set 1	Normal	150	10.0	Normal	4	1	0.16
Set 2	Normal	50	7.0	Normal	3	0.7	0.25

To exemplify this potential, we used DuMu^x FracLab to upscale the elastic properties and the permeability of the fractured rock mass presented by Yang et al. (2014) using Dirichlet (linear displacement/linear pressure), Neumann (constant tractions/flux) and periodic boundary conditions. Table 5 describes the statistical properties of the fracture Network and Fig. 15 shows an example of a sample and the adopted finite element mesh. We generated 100 different random fractured rock masses that respect these statistical distributions, and for each generation sample sizes from 4 m x 4 m to 20 m x 20 m were tested. The process for generating the samples is described in Loyola et al. (2021). Table 6 presents the elastic parameter and permeabilities adopted for the intact rock and the fractures.

Figs. 16 and 17 present the average smallest and the largest eigenvalues of the permeability and the elastic compliance tensor as a function of sample size. The Dirichlet, Neumann and periodic boundary conditions continue to return highest, lowest and intermediary values for the average properties. However, it is not evident which boundary condition returns the fastest convergence of the properties with sample size, as is the case for true periodic media. Also, the three types of boundary condition return quite similar Coefficient of Variations (COVs) for the properties (Figs. 18 and 19), which suggests that they would require similar REV sizes when using variability-based criteria (e.g., Min and Jing, 2003; Farahmand et al., 2018; Loyola et al., 2021).

Table 6
Elastic properties and permeability for the intact rock and the fractures used to compare linear Dirichlet, Neumann and periodic boundary conditions.

Intact rock			Fracture		
E (GPa)	ν	$k_m(m^2)$	K_n (GPa/m)	K_t (GPa/m)	$k_f(m^2)$
50.0	0.25	1.0×10^{-14}	50.0	10.0	3.5×10^{-10}

5.2. Example 2: Permeability history of a fractured sample submitted to depletion and triaxial extension

The poromechanical behavior of fractures impacts activities such as the exploitation of naturally fractured reservoirs, where continual effective stress changes provoked by depletion or injection can induce fracture deformation and, consequently, permeability changes.

To exemplify this, we simulate the experimental program conducted by Teufel et al. (1993) on fractured core samples of the chalk in the Ekofisk reservoir. Their samples were crossed by one unfilled subvertical fracture that is typical of the shear fractures in the Ekofisk. The samples were initially loaded to a confinement lateral stress of 55 MPa and an axial stress of 72 MPa and had an initial pore pressure of 48 MPa. After the confinement, the samples were subjected to depletion combined with triaxial extension. To induce depletion, the pore pressure was reduced by 3.45 MPa every 2 h. Simultaneously, the lateral confinement stress was decreased in such a way that the effective stress path would follow a certain K ratio given by:

$$K = \frac{\Delta\sigma'_h}{\Delta\sigma'_v} = \frac{\Delta p}{\Delta p + \Delta\sigma_h} \tag{37}$$

where $\Delta\sigma'_h$ and $\Delta\sigma'_h$ are the variations of lateral and vertical effective stresses, respectively, Δp is the pore pressure increment of −3.45 MPa

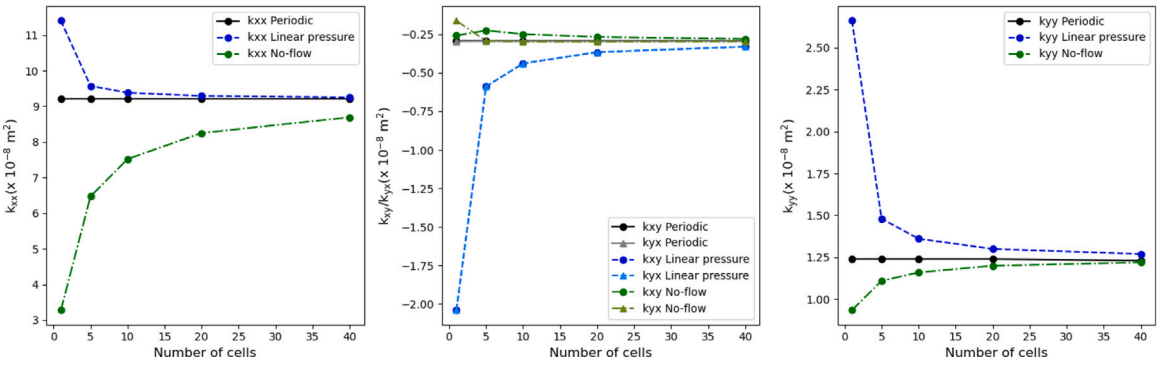

Fig. 13. Validation Test 5: Comparison of the upscaled components of the permeability tensors when using linear pressure, flux and mortar periodic boundary conditions.

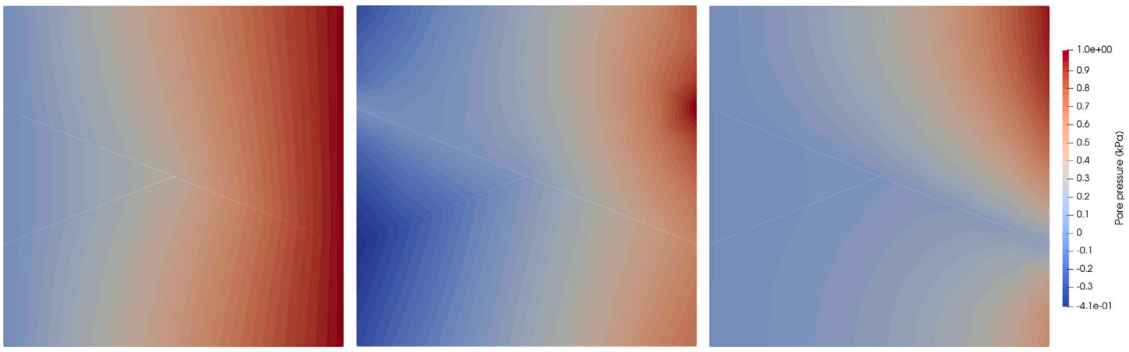

Fig. 14. Comparison of the pressure fields inside the unit cell of Fig. 12 when using linear pressure (left), mortar periodic (center), and flux (right) boundary conditions to impose a pressure gradient of 1kPa/m or flux of 8.33×10^{-6} m/s (for the flux) in the x-direction. For the periodic case, the master corner is the lower right one and it was imposed to a pressure of 0.7 kPa.

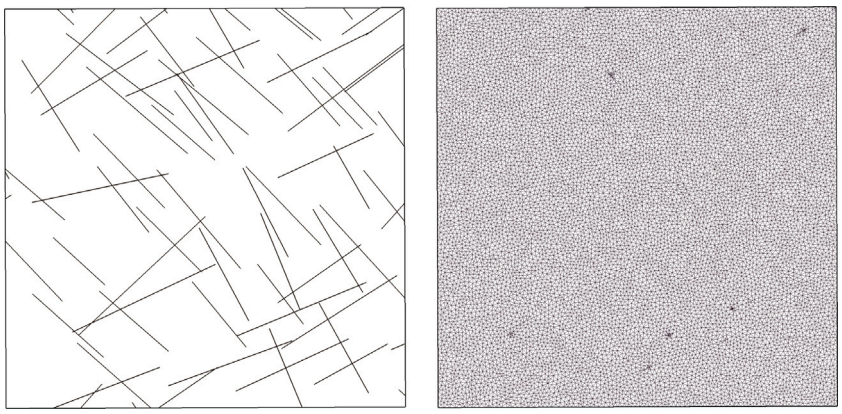

Fig. 15. Numerical example 1: example of one of the generated fracture networks and the adopted mesh.

and $\Delta\sigma_h$ is the total lateral stress variation that needs to be applied to follow the desired K ratio. Three values of K were tested: 1.0, 0.5 and 0.2. After each pore pressure decrement, Teufel et al. (1993) waited for a stabilization period and then conducted permeability tests to obtain the history of apparent axial permeability history.

To reproduce this problem in DuMu^x, we used a sample similar to the one of Validation Test 2 (Fig. 8) where the fracture makes an angle α of 17° with the axial direction, which was the orientation reported by Teufel et al. (1993) for their samples. The simulation is composed of two stages: the first one is a confinement stage, where the sample is loaded to the initial stress state of the lab experiments; and the second one is the depletion and triaxial extension phase, where the pore pressure and lateral stress variations are applied. By the end of the confinement phase and of each pore pressure decrement of 3.5 MPa, the permeability upscaling method in the Homogenization module of DuMu^x FracLab is called to compute the equivalent permeability of the sample with linear pressure boundary conditions.

In the numerical model, the intrinsic permeability k_f of the fracture is described by the cubic law:

$$k_f = \frac{w^2}{12} \tag{38}$$

where w is the fracture's aperture. And the fracture's normal stiffness K_n is described as a function of the normal displacement jump $[[u_n]]$ by the Barton-Bandis law (Barton et al., 1985), according to which:

$$K_n = \frac{K_{ni}}{\left(1 + \frac{u_n}{u_{max}}\right)^2} \tag{39}$$

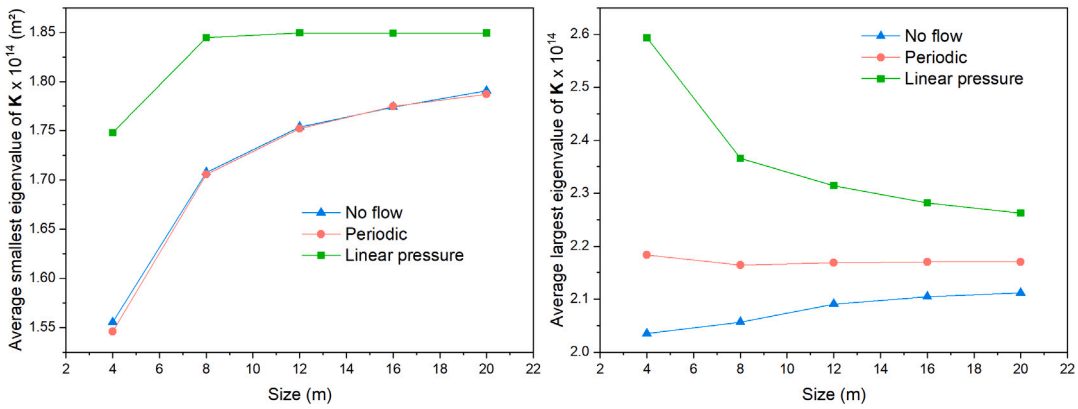

Fig. 16. Numerical example 1: Average value of the eigenvalues of the equivalent permeability tensor $\boldsymbol{K}$ when using linear pressure, periodic and flux conditions.

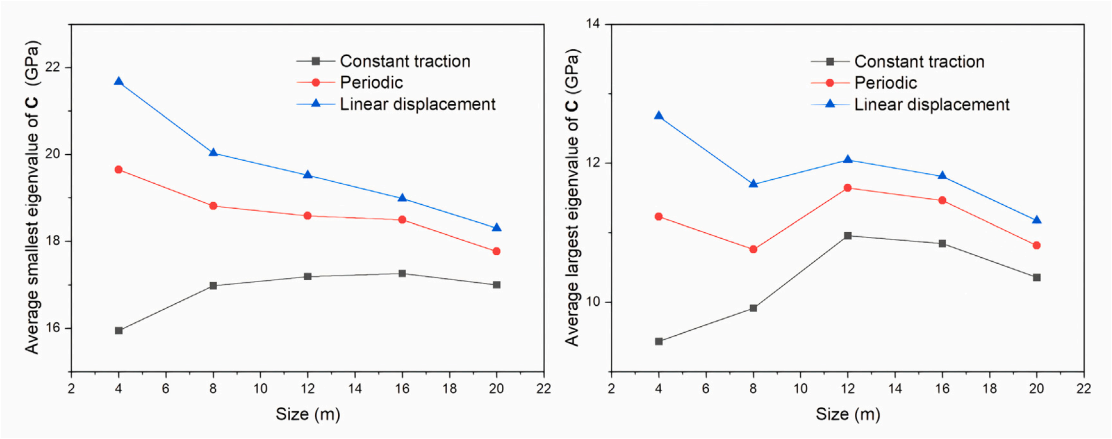

Fig. 17. Numerical example 1: Average value of the eigenvalues of the equivalent stiffness tensor $\boldsymbol{C}$ when using linear displacements, periodic and constant traction boundary conditions.

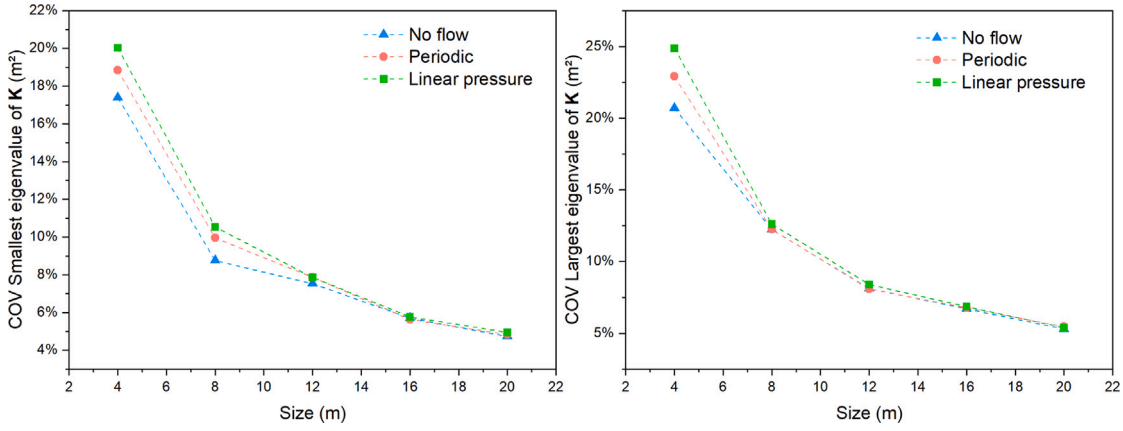

Fig. 18. Numerical example 1: COV of the eigenvalues of the equivalent permeability tensor $\boldsymbol{K}$ when using linear pressure, periodic and flux conditions.

where K_{ni} is the initial normal stiffness, u_n is the normal displacement jump (here positive for traction or opening) and u_{max} is the fractures maximum closure.

Both the fractures and the matrix are described by a Mohr–Coulomb criterion. Table 7 presents the material parameters. The matrix permeability is taken from the experimental measurements (Teufel et al., 1993) and it is stress-dependent in the model. Following the measurements by the authors, it varies from 1.2 mD to 0.5 mD from an effective mean stress of 7 MPa to 55 MPa. All the other parameters, except for the fracture's strength parameters, were taken from Gutierrez et al. (1994), who studied the mechanical behavior of samples of the same fractured chalk. The porous matrix properties are those reported for a porosity of 30% of porosity, which is the porosity of the rock matrix tested by Teufel et al. (1993). The Mohr–Coulomb parameters of the fracture were calibrated to fit the permeability evolution of the path $K = 0.2$ (Fig. 20), which was the only one to present shear yielding. To avoid matrix singularity problems that are typical of numerical models that employ perfectly plastic models with stress boundary conditions, we

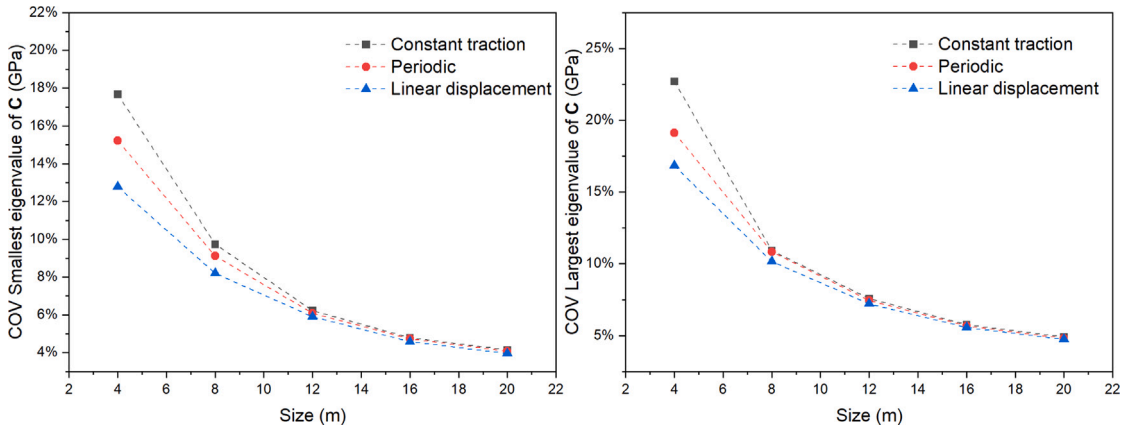

Fig. 19. Numerical example 1: COV of the eigenvalues of the equivalent stiffness tensor $\boldsymbol{C}$ when using linear displacements, periodic and constant traction boundary conditions.

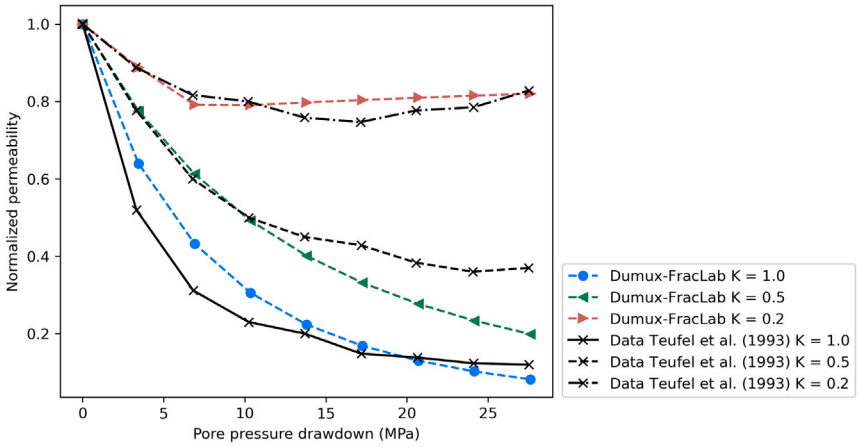

Fig. 20. Numerical example 2: Comparison of the normalized permeability history obtained in the laboratory by Teufel et al. (1993) and in the numerical simulation with DuMu^x FracLab for different values of stress ratio K.

Table 7
Numerical example 2: poroelastic parameters of the porous matrix and the fracture.

Matrix					
E (GPa)	ν	k_m (mD)	c (GPa)	ϕ (°)	ψ (°)
6.8	0.14	1.2	12.0	50	0

Fracture						
K_{ni} (GPa/m)	K_t (GPa/m)	K_{nl} (GPa/m)	w_0 (mm)	c_f (GPa)	ϕ_f (°)	ψ_f (°)
10	50	0	1.38	0.1	20	0.47

used the strain-hardening Mohr–Coulomb to apply a slight hardening. For that, cohesion was set to be a linear function of the plastic shear displacement jump at a rate of 0.01 GPa/m. Thus, this problem also exemplifies how to set a new state variable to be stored in DuMu^x, and also how to use it to update the strength parameters.

Fig. 20 presents the normalized permeability evolution obtained in the numerical model and in the laboratory. The numerical model can capture the initially steeper permeability decrease when $K = 1.0$ and 0.5. This behavior is due to the Barton-Bandis model, which makes fractures stiffer as they close and thus provoke smaller permeability changes as depletion proceeds. The behavior of the sample when $K = 0.2$ is also well captured: there is an initial permeability decrease, but once the fracture yields it dilates under shear, which provokes a regain of permeability. As in the numerical laboratory, this is the only sample to shear during the triaxial extension and depletion tests.

In this model, due to the high initial aperture, the fractures remain more permeable than the matrix at the end of the depletion. To better demonstrate what could be the effect of significant fracture deformation on the hydraulic behavior of the sample, Fig. 21 presents the pore pressure fields of a sample submitted to upwards flow rate when $w_0 = 0.1$ mm and $K = 1$. There is a clear change of behavior: while in the beginning of depletion the fracture acts as a preferential path for flow and induces anisotropy by provoking a visible pressure gradient in the x-direction, by the end of the depletion the pressure fields are close to what would be expected for a homogeneous sample.

6. Conclusions, limitations and perspectives

We presented a code that successfully applies the Box method for the first time in elastoplastic analyses of fractured media. Also, it contains functionalities that are useful for the homogenization and the upscaling of constitutive tensors of heterogeneous domains with Dirichlet, Neumann and periodic boundary conditions. For these latter, we implemented a recent method that permits the imposition of periodic boundary conditions on general meshes and modified it to work with meshes with triple-nodded interfaces. The verification test 5 and the Numerical Example 1 demonstrate that, as theoretically expected, Neumann, Dirichlet and periodic boundary return lower, intermediary and upper values for the upscaled properties. Also, the Numerical Example 2 demonstrates that the formulations available

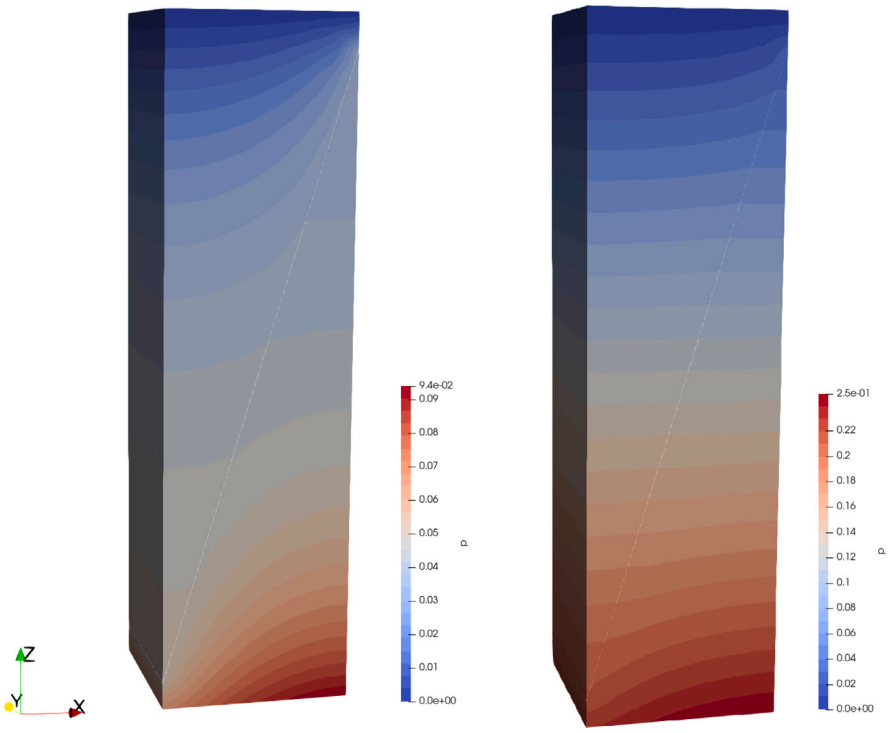

Fig. 21. Numerical example 2: Pore pressure fields of the fractured sample submitted to an upward flux at the start (left) and end (right) of depletion when $w_0 = 0.1$ mm.

in DuMu^x FracLab, including the hydromechanical coupling, the nonlinear elasticity and the Mohr–Coulomb criterion for the fractures, are useful to reproduce the behavior of real rock samples.

DuMu^x FracLab is an open source platform that users can hopefully improve and extend. There are current limitations that can be addressed to move towards making DuMu^x as robust for the simulation of coupled elastoplastic problems as it is for the simulation of complex flow and transport processes.

We did not make changes on the original way DuMu^x performs system assembly with the perturbation method, but it has drawbacks. Firstly, when it comes to elastoplastic problems, it can face efficiency issues for requiring the return algorithm to be recalled for each perturbation, when in the plastic regime. Second, there might be convergence issues. The convergence of the simulations has showed to be very sensitive to the selected perturbation in elastoplastic problems, so a possible improvement would be to implement consistent tangent operators (Simo and Taylor, 1985) that may employ the finite element shape functions to compute derivatives or use perturbation methods specifically idealized for inelasticity (e.g., Miehe, 1996).

The implementation of other constitutive plastic models than the Mohr–Coulomb criterion would also be welcome. The design of the plastic correction classes make this implementation easy, but more complex models could also require further development in other areas, such as the solution scheme. For example, when working with damage mechanics and strain-softening, an efficient explicit scheme may be desirable.

Another interesting perspective for DuMu^x FracLab is to add new coupling managers that would handle the coupling of geomechanics with other DuMu^x models. While the new module currently allows for coupling with one-phase flow only, DuMu^x can deal with multi-phase and multi-compositional flow, transport and thermal problems, all of which can significantly interact with the mechanical behavior.

CRediT authorship contribution statement

Ana Carolina Loyola: Formal analysis, Investigation, Methodology, Software, Validation, Writing – original draft, Writing – review & editing. **Manoel Porfírio Cordão Neto:** Methodology, Supervision, Writing – original draft, Writing – review & editing. **Jean-Michel Pereira:** Methodology, Supervision, Writing – original draft, Writing – review & editing.

Declaration of competing interest

The authors declare that they have no known competing financial interests or personal relationships that could have appeared to influence the work reported in this paper.

Data availability

The code and all the examples are open-source/open-access and available in the git repository in the article.

Acknowledgments

This work was finantially supported by the Coordenação de Aperfeiçoamento de Pessoal de Nível Superior - CAPES and the Conselho Nacional de Desenvolvimento Científico e Tecnológico - CNPq. This support is gratefully acknowledged.

References

Bandis, S., 1980. Experimental Studies of Scale Effects on Shear Strength, and Deformation of Rock Joints (Ph.D. thesis). University of Leeds.

Barton, N., Bandis, S., Bakhtar, K., 1985. Strength, deformation and conductivity coupling of rock joints. Int. J. Rock Mech. Min. Sci. Geomechan. Abstracts 22 (3), 121–140.

Berre, I., Boon, W.M., Flemisch, B., Fumagalli, A., Gläser, D., Keilegavlen, E., Scotti, A., Stefansson, I., Tatomir, A., Brenner, K., Burbulla, S., Devloo, P., Duran, O., Favino, M., Hennicker, J., Lee, I.-H., Lipnikov, K., Masson, R., Mosthaf, K., Nestola, M.G.C., Ni, C.-F., Nikitin, K., Schädle, P., Svyatskiy, D., Yanbarisov, R., Zulian, P., 2021. Verification benchmarks for single-phase flow in three-dimensional fractured porous media. Adv. Water Resour. 147, 103759. http://dx.doi.org/10.1016/j.advwatres.2020.103759.

Bilke, L., Fischer, T., Naumov, D., Lehmann, C., Wang, W., Lu, R., Meng, B., Rink, K., Grunwald, N., Buchwald, J., Silbermann, C., Habel, R., Günther, L., Mollaali, M., Meisel, T., Randow, J., Einspänner, S., Shao, H., Kurgyis, K., Kolditz, O., Garibay, J., 2022. OpenGeoSys. http://dx.doi.org/10.5281/zenodo.7092676, Zenodo.

Castelletto, N., White, J., Tchelepi, H., 2015. Accuracy and convergence properties of the fixed-stress iterative solution of two-way coupled poromechanics. Int. J. Numer. Anal. Methods Geomech. 39 (14), 1593–1618.

Castro, E.S., Barroso, J.S., Murad, M.A., Guerreiro, J.N., 2023. Reduced flow model and transmissibility upscaling in multi-layered faulted reservoirs. Comput. Geosci. 105439. http://dx.doi.org/10.1016/j.cageo.2023.105439.

Cerfontaine, B., Dieudonné, A., Radu, J., Collin, F., Charlier, R., 2015. 3D zero-thickness coupled interface finite element: Formulation and application. Comput. Geotech. 69, 124–140. http://dx.doi.org/10.1016/j.compgeo.2015.04.016.

Chalon, F., Mainguy, M., Longuemare, P., Lemonnier, P., 2004. Upscaling of elastic properties for large scale geomechanical simulations. Int. J. Numer. Anal. Methods Geomech. 28 (11), 1105–1119.

Chen, B., Barboza, B.R., Sun, Y., Bai, J., Thomas, H.R., Dutko, M., Cottrell, M., Li, C., 2022. A review of hydraulic fracturing simulation. Arch. Comput. Methods Eng. 29, 1–58. http://dx.doi.org/10.1007/s11831-021-09653-z.

Crisfield, M.A., 1987. Plasticity computations using the mohr—coulomb yield criterion. Eng. Comput. 4 (4), 300–308.

Cui, W., Potts, D.M., Zdravković, L., Gawecka, K.A., Tsiampousi, A., 2019. Formulation and application of 3D THM-coupled zero-thickness interface elements. Comput. Geotech. 116, 103204. http://dx.doi.org/10.1016/j.compgeo.2019.103204.

de Souza Neto, E., Blanco, P., Sánchez, P., Feijóo, R., 2015. An RVE-based multiscale theory of solids with micro-scale inertia and body force effects. Mech. Mater. 80, 136–144. http://dx.doi.org/10.1016/j.mechmat.2014.10.007.

Duncan, J.M., Goodman, R.E., 1968. Finite Element Analyses of Slopes in Jointed Rock: A Report of an Investigation. Technical Report, (S-68-3), U.S. Army Corps of Engineers.

Esmaieli, K., Hadjigeorgiou, J., Grenon, M., 2010. Estimating geometrical and mechanical REV based on synthetic rock mass models at Brunswick Mine. Int. J. Rock Mech. Min. Sci. 47, 915–926.

Farahmand, K., Vazaios, I., Diederichs, M.S., Vlachopoulos, N., 2018. Investigating the scale-dependency of the geometrical and mechanical properties of a moderately jointed rock using a synthetic rock mass (SRM) approach. Comput. Geotech. 95, 162–179.

Flemisch, B., Berre, I., Boon, W., Fumagalli, A., Schwenck, N., Scotti, A., Stefansson, I., Tatomir, A., 2018. Benchmarks for single-phase flow in fractured porous media. Adv. Water Resour. (111), 239–258.

Gan, Q., Elsworth, D., 2016. Production optimization in fractured geothermal reservoirs by coupled discrete fracture network modeling. Geothermics 62, 131–142.

Gläser, D., 2020. Discrete Fracture Modeling of Multi-Phase Flow and Deformation in Fractured Poroelastic Media (Ph.D. thesis). Universität Stuttgart. - Stuttgart: Institut für Wasser- und Umweltsystemmodellierung.

Goodman, R., Taylor, R., Brekke, T., 1968. A model for the mechanics of jointed rock. J. Soil Mech. Found. Div. 94.

Gutierrez, M., Tunbridge, L., Hansteen, H., Makurat, A., Barton, N., Landa, G.H., 1994. Modelling of the compaction behaviour of fractured chalk. In: SPE/ISRM Rock Mechanics in Petroleum Engineering, All Days. SPE-28130-MS.

Helmig, R., 1997. Multiphase Flow and Transport Processes in the Subsurface: A Contribution to the Modeling of Hydrosystems. Springer-Verlag, Berlin, Germany.

Hill, R., 1972. On constitutive macro-variables for heterogeneous solids at finite strain. Proc. R. Soc. Lond. Ser. A Math. Phys. Eng. Sci. 326, 131–147.

Jaeger, J.C., 1960. Shear failure of anistropic rocks. Geol. Mag. 97 (1), 65–72. http://dx.doi.org/10.1017/S0016756800061100.

JianPing, Y., WeiZhong, C., DianSen, Y., JingQiang, Y., 2015. Numerical determination of strength and deformability of fractured rock mass by FEM modeling. Comput. Geotech. 64, 20–31.

Khoei, A., Hajiabadi, M.R., 2018. Fully coupled hydro-mechanical multi-scale model with micro-dynamic effects. Internat. J. Numer. Methods Engrg. 115 (3), 1–35.

Khoei, A.R., Saeedmonir, S., Misaghi Bonabi, A., 2023. Computational homogenization of fully coupled hydro-mechanical analysis of micro-fractured porous media. Comput. Geotech. 154, 105121. http://dx.doi.org/10.1016/j.compgeo.2022.105121.

Kim, J., Tchelepi, H., Juanes, R., 2011. Stability and convergence of sequential methods for coupled flow and geomechanics: Fixed-stress and fixed-strain splits. Comput. Methods Appl. Mech. Engrg. 200 (13), 1591–1606.

Koch, T., Gläser, D., Weishaupt, K., Ackermann, S., Beck, M., Becker, B., Burbulla, S., Class, H., Coltman, E., Emmert, S., Fetzer, T., Grüninger, C., Heck, K., Hommel, J., Kurz, T., Lipp, M., Mohammadi, F., Scherrer, S., Schneider, M., Seitz, G., Stadler, L., Utz, M., Weinhardt, F., Flemisch, B., 2020. DuMux 3 – an open-source simulator for solving flow and transport problems in porous media with a focus on model coupling. Comput. Math. Appl. 81, 423–443.

Larsson, F., Runesson, K., Su, F., 2011. Computational homogenization of uncoupled consolidation in micro-heterogeneous porous media. Int. J. Numer. Anal. Methods Geomech. 34, 1431–1458.

Liaudat, J., Dieudonné, A.-C., Vardon, P.J., 2023. Modelling gas fracturing in saturated clay samples using triple-node zero-thickness interface elements. Comput. Geotech. 154, 105128. http://dx.doi.org/10.1016/j.compgeo.2022.105128.

Long, J.C., Remer, J.S., Wilson, C.R., Witherspoon, P.A., 1982. Porous media equivalents for networks of discontinuous fractures. Water Resour. Res. 18 (3), 645–658.

Loyola, A., Pereira, J., Cordão Neto, M., 2021. General statistics-based methodology for the determination of the geometrical and mechanical representative elementary volumes of fractured media. Rock Mech. Rock Eng. 54 (4), 1821–1841.

Mandel, J., 1953. Consolidation Des Sols (Étude Mathématique). Géotechnique 3 (7), 287–299.

Martínez, A., Liaudat, J., López, C.M., Carol, I., 2022. 3D zero-thickness interface model for fracture of cement-based materials with chemical degradation. Int. J. Solids Struct. 238, 111379. http://dx.doi.org/10.1016/j.ijsolstr.2021.111379.

Massart, T., Selvadurai, P., 2012. Stress-induced permeability evolution in a quasi-brittle geomaterial. J. Geophys. Res. (Solid Earth) 117, B07207.

Miehe, C., 1996. Numerical computation of algorithmic (consistent) tangent moduli in large-strain computational inelasticity. Comput. Methods Appl. Mech. Engrg. 134 (3), 223–240. http://dx.doi.org/10.1016/0045-7825(96)01019-5.

Miehe, C., 2003. Computational micro-to-macro transitions for discretized micro-structures of heterogeneous materials at finite strains based on the minimization of averaged incremental energy. Comput. Methods Appl. Mech. Engrg. 192 (5), 559–591.

Min, K., Jing, L., 2003. Numerical determination of the equivalent elastic compliance tensor for fractured rock masses using the distinct element method. Int. J. Rock Mech. Min. Sci. 40, 795–816.

Nayak, G.C., Zienkiewicz, O.C., 1972. Elasto-plastic stress analysis. A generalization for various contitutive relations including strain softening. Internat. J. Numer. Methods Engrg. 5 (1), 113–135.

Nguyen, V.-D., Béchet, E., Geuzaine, C., Noels, L., 2012. Imposing periodic boundary condition on arbitrary meshes by polynomial interpolation. Comput. Mater. Sci. 55, 390–406.

Pouya, A., 2015. A finite element method for modeling coupled flow and deformation in porous fractured media. Int. J. Numer. Anal. Methods Geomech. (39), 1836–1852.

Pouya, A., Fouché, O., 2009. Permeability of 3D discontinuity networks: New tensors from boundary-conditioned homogenisation. Adv. Water Resour. 32 (3), 303–314.

Pouya, A., Ghoreychi, M., 2001. Determination of rock mass strength properties by homogenization. Int. J. Numer. Anal. Methods Geomech. 25 (13), 1285–1303.

Preisig, M., Prevost, J., 2011. Coupled multi-phase thermo-poromechanical effects. Case study: CO 2 injection at in salah, Algeria. Int. J. Greenh. Gas Control 5, 1055–1064. http://dx.doi.org/10.1016/j.ijggc.2010.12.006.

Reis, F., Andrade Pires, F., 2014. A mortar based approach for the enforcement of periodic boundary conditions on arbitrarily generated meshes. Comput. Methods Appl. Mech. Engrg. 274, 168–191.

Rodrigues Lopes, I., Ferreira, B., Andrade Pires, F., 2021. On the efficient enforcement of uniform traction and mortar periodic boundary conditions in computational homogenisation. Comput. Methods Appl. Mech. Engrg. 384, 113930.

Rutqvist, J., Rinaldi, A.P., Cappa, F., Moridis, G.J., 2013. Modeling of fault reactivation and induced seismicity during hydraulic fracturing of shale-gas reservoirs. J. Pet. Sci. Eng. 107, 31–44. http://dx.doi.org/10.1016/j.petrol.2013.04.023.

Rutqvist, J., Stephansson, O., 2003. The role of hydrochemical coupling in fractured rock engineering. Hydrogeol. J. 11, 7–40.

Segura, J., Carol, I., 2004. On zero-thickness elements for diffusion problems. Int. J. Numer. Anal. Methods Geomech. 28, 947–962.

Segura, J., Carol, I., 2008a. Coupled HM analysis using zero-thickness interface elements with double nodes—Part II: Verification and application. Int. J. Numer. Anal. Methods Geomech. 32, 2103–2123. http://dx.doi.org/10.1002/nag.730.

Segura, J., Carol, I., 2008b. Coupled HM analysis using zero-thickness interface elements with double nodes. Part I: Theoretical model. Int. J. Numer. Anal. Methods Geomech. (32), 2083–2101.

Simo, J., Taylor, R., 1985. Consistent tangent operators for rate-independent elastoplasticity. Comput. Methods Appl. Mech. Engrg. 48 (1), 101–118. http://dx.doi.org/10.1016/0045-7825(85)90070-2.

Svenning, E., Fagerström, M., Larsson, F., 2016. Computational homogenization of microfractured continua using weakly periodic boundary conditions. Comput. Methods Appl. Mech. Engrg. 299, 1–21.

Tao, Q., Ghassemi, A., Ehlig-Economides, C.A., 2011. A fully coupled method to model fracture permeability change in naturally fractured reservoirs. Int. J. Rock Mech. Min. Sci. 48 (2), 259–268.

Terada, K., Hori, M., Kyoya, T., Kikuchi, N., 2000. Simulation of the multi-scale convergence in computational homogenization approaches. Int. J. Solids Struct. 37 (16), 2285–2311.

Teufel, L., Rhett, D., Farrell, H., Lorenz, J., 1993. Control of fractured reservoir permeability by spatial and temporal variations in stress magnitude and orientation. In: SPE Annual Technical Conference and Exhibition.

Yang, J., Chen, W., Y., D., Yu, H., 2014. Numerical determination of elastic compliance tensor of fractured rock masses by finite element modeling. Int. J. Rock Mech. Min. Sci. 70, 474–482.